AUT Journal of Electrical Engineering

AUT J. Elec. Eng., 52(2) (2020) 187-192
DOI: 10.22060/eej.2020.18179.5346

Development of a free anthropomorphic voxel model of human body for wide-band computational electromagnetics dosimetry

M. Rajaei Golsefidi [1], Z. Hajizadeh Bakhtiary[2], E. Sharifi[2], M. Saviz[2,*], R. Faraji-Dana[3]

[1] School of Electrical and Computer Engineering, University of Tehran
[2] Biomedical Engineering Department, Amirkabir University of Technology (Tehran Polytechnic)
[3] Center of Excellence on applied Electromagnetic Systems, School of Electrical and Computer Engineering, University of Tehran

ABSTRACT: To calculate and evaluate wave scattering and penetration of electromagnetic waves in different biological tissues it is necessary to use a realistic model of the human body, with all tissues resolved and separately assigned with appropriate electric/magnetic properties. We report the development of a realistic 3D whole-body human model that has been adapted for simulation in CST software, containing 46 different resolved tissues with their relevant electrical properties over 1Hz-100 GHz, non-ionizing electromagnetic radiation. The model is based on whole-body magnetic resonance images (MRI) of Zubal-phantom data with voxel dimensions of 3.6 mm. Wideband simulations are performed to show the successful application of the model in computational dosimetry. The results of the electric field calculation indicate that the peak of electric field in the body occurs at around 70 MHz, which is the same as the well-known resonant frequency of the body. Moreover, the difference between electric field intensity among tissues can be as high as 30 dB, and that tissues with lower water content (e.g. bones, knee) can generally have higher induced electric fields. High water content tissues such as the eye vitreous humor have generally lower induced electric fields. The model is available free of charge for research purposes at bioelectromag.ir.

Review History:
Received: 2020-03-30
Revised: 2020-07-02
Accepted: 2020-07-05
Available Online: 2020-12-01

Keywords:
MRI images
voxel model
anthropomorphic model
dosimetry

1.Introduction

Interactions of electromagnetic field (EMF) with human body is an important issue in the field of biomedical research and safety assessment. The use of realistic voxel models of the entire human body has been much in demand for computational dosimetry of non-ionizing electromagnetic waves[1]. There are several human models available from commercial sources, such as the virtual population from IT'IS [2], and the NORMAN model [3] or the Austinman/ woman [4], NAOMI [5] and the florida children voxel model [6] and other national models[7]. Most of these are however, of limited availability and are not free. Some researchers have tried to create shape-deformable models that can be used to create different models for different postures of human body [8]. Models can be voxel-based or based on polyhedral meshcells. However, voxel models fit conceptually with the FDTD Method or its derivative stabilized method of FIT. Consequently, voxel models are very often employed for dosimetric evaluations[9].

The purpose of the research reported here was to construct a free realistic whole-body voxel models based on MRI data over as wide a frequency range as possible (1Hz-10GHz) that can be easily used in CST computational electromagnetics software. Our model is based on Zubal's whole-body (arms down) phantom [10]. This is a voxel model based on MRI images with 125 tissue resolved with 192×96×498 bytes volume. The model has no electrical properties and these had to be added. The merit and novelty of our model is (1) it is distributed herein as free for research purposes and (2) In absence of electrical properties for many of the 125 tissues in the Zubal phantom, we have established carefully-selected corresponding tissues for them, as described in the material s and methods section together with many other challenges that has been solved. Finally, we show full-wave computations of plane waves incident on human body over 1 Hz- 10 GHz, to see how different tissues differ in the amount of induced electric fields at different frequencies. Frequency responses of all tissues have been computed and plotted.

*Corresponding author's email: msaviz@aut.ac.ir

2. Model Development

Zubal's whole-body (arms down) phantom from the free-source visible human project [10] was taken and the data files were interpreted into a 3D matrix of tissue numbers. Each entry in this matrix corresponds to a voxel in the actual human body model. The entries are tissue numbers. Some changes were implemented in the Zubal model to make it appropriate for electromagnetic simulation in CST studio. First, the format of model files were changed to match a proper format for simulation in CST studio. Second, the electrical properties of more than 125 tissues available in the zubal model had to be determined. In the CST format, each

frequency has to be assigned a file, in which the properties for all tissue numbers have to be given. These tissue properties are conventionally found from the 4-cole-cole model based on the data by Gabriel et al.[11-13].

$$\varepsilon_r = \sum_{i=0}^{4} \frac{\Delta\varepsilon_i}{1 + (j\omega\tau_i)^{1-\alpha_i}} + \frac{\sigma_{ionic}}{j\omega\varepsilon_0} \quad (1)$$

Where σ_{ionic} is the ionic (DC) conductivity of the tissue, ω is the angular frequency in rad/s and the rest are parameters given by [11] for all tissues. All thermal, physical, and dielectric parameters are taken from IT'IS database, available at [14]. Electrical properties were compiled in separate data files in proper formats. As a challenge, the electrical properties of many tissues in zubal model are not available in the literature. We match these with available and equivalent tissues that are close to the desired tissue either in terms of function or structure. The final results of the tissue matching process for this model are summarized in table 1.

Other points to consider include:

• There is no data available in the literature for the dielectric properties of urine over the frequency spectrum of single Hz to a few GHz mandatory for fitting to the 4-cole-cole dispersion model. Therefore, for the dielectric parameter values of urine, IT'IS has chosen the values for th e urinary bladder wall, and for the thermal properties, the mean value of bladder wall and urine is calculated.

• The dielectric properties database generated by Gabriel et al., 1996 [13] contains values for only a few endocrine tissues: thyroid, testes, and ovaries. For all reproductive organs, the values reported for testes and, for all other glands, those of thyroid is used.

• The contents of the stomach and intestines depend on the diet of the subject. For the thermal properties, an average of water and muscle corresponding to a diet of 50/50 water and meat is calculated. For the dielectric properties, IT'IS has chosen the values for muscle only.

This model consists of 243x128x128 cubic voxels, all of 3.6 mm dimension in the adult phantom. Fig. 1 shows the developed whole-body voxel model. This model is in the arms down position, as if standing on the ground with the hands at the sides of body.

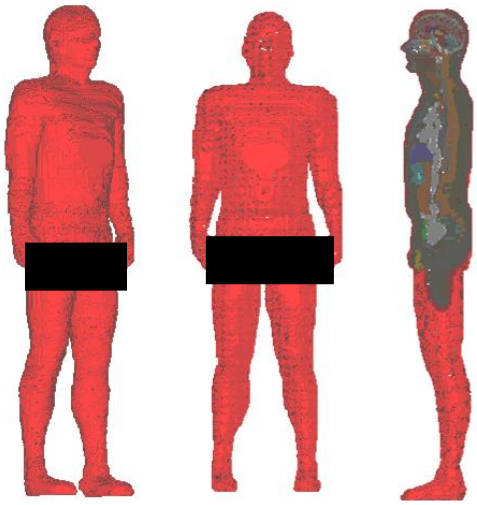

Fig. 1.The view of whole-body voxel model of human in cst.

Fig. 2. Sample demonstration of the segmented cross-section in the Zubal model.

3. Application to electromagnetic dosimetry

3-1- Simulation Settings

The developed human body model was used to obtain the frequency response functions for all tissues and organs of the body (heart, kidney, etc.) in the entire 1 kHz to 1 GHz frequency band using the CST-MWS software.

The radiation model is an E-polarized (Electric field vector along body axis) plane wave that is incident on the body from front and has an electric field intensity of 1 V/m at all frequencies. Practically this corresponds to the person being in the far field of a transmitting antenna; e.g. from the base transceiver stations (BTS) antennas at distances greater than 200 meters.

Induced electric fields are solved using full wave electromagnetic equations (Maxwell's equations). Open boundary conditions were applied with placing solids (filled with vacuum) around the model to distance from absorbing boundary conditions. Convergence has been checked for all simulations.

3-2 Results

The first-attempt results of the electric field are presented in Fig. 3 Accordingly, it is seen that the field is different in different tissues and varies with frequency. The discontinuity in some tissues at 100 kHz is because the two frequency bands (1kHz-100kHz) and (100 kHz-1GHz) were simulated separately considering software limitations. Although both results converge, slight misalignments such as these were found to occur nevertheless, due to the insignificant properties of materials at the fitting level, the number of meshes, the number of excitation pulses in two simulations, and the computational accuracy of the software. The solutions to eliminate this difference are discussed next.

To correct the frequency response at 100 kHz and lower, we applied the following line of reasoning: The range below 1MHz corresponds to *quasi-static* conditions. It is known that in quasi-static conditions, fields induced inside bounded objects (either by time-varying magnetic component or by the time varying electric component) tends to increase with frequency by first order (f). Consequently it is reasonable to expect a rise of 20dB/decade in E with rising frequency.

Table 1. Tissue matching summary and the tissue numbers in the final CST Model

Zubal's voxel number	Zubal's tissue name	CST voxel number	CST tissue name	Zubal's voxel number	Zubal's tissue name	CST voxel number	CST tissue name
0	outside phantom	1	Air	76	hard palate	4	Bone
1	skin	34	Skin	77	cerebellum	11	Cerebellum
2	brain	7	Brain	78	tongue	43	Tongue
3	spinal cord	37	Spinal Cord	81	horn of mandible	4	Bone
4	skull	35	Skull	82	nasal septum	4	Bone
5	spine	37	Spinal Cord	83	white matter	9	Brain White Matter
6	rib cage & sternum	5	Bone Cancellous	84	superior sagittal sinus	1	Air
7	pelvis	5	Bone Cancellous	85	medulla oblongata	26	Medulla Oblongata
8	long bones	6	Bone Cortical	88	artificial lesion	3	Blood
9	skeletal muscle	27	Muscle	89	frontal lobes	8	Brain Grey Matter
10	lungs	25	Lung	91	pons	32	Pons
11	heart	27	Muscle	92	third ventricle	12	Cerebrospinal Fluid
12	liver	24	Liver	94	pineal body	31	Pineal Body
13	gallbladder	19	Gallbladder	95	occipital lobes	8	Brain Grey Matter
14	kidney	22	Kidney	96	hippocampus	20	Hippocampus
15	Pharynx	30	Pharynx	97	pituitary gland	21	Hypophysis
16	esophagus	15	Esophagus	98	fat (head)	18	Fat
17	stomach	39	Stomach	99	uncus (ear bones)	10	Cartilage
18	small bowel	36	Small Intestine	100	turbinates	4	Bone
19	colon	23	Large Intestine	101	caudate necleus	7	Brain
20	pancreas	29	Pancreas	102	zygoma	4	Bone
21	adrenals	2	Adrenal Glands	103	insula cortex	8	Brain Grey Matter
22	fat	18	Fat	104	sinuses/mouth cavity	1	Air
23	blood pool	3	Blood	105	putamen	7	Brain
24	gas (bowel)	1	Air	106	optic nerve	28	Nerve
25	fluid (bowel)	3	Blood	107	internal capsule	9	Brain White Matter
26	bone marrow	4	Bone	108	septum pellucidum	7	Brain
28	thyroid	42	Thyroid Gland	109	thalamus	41	Thalamus
29	trachea	45	Trachea	110	eyeball	17	Eye Vitrous Humor
30	Cartilage	10	Cartilage	111	corpus collosum	9	Brain White Matter
31	spleen	38	Spleen	112	special region frontal lobes	8	Brain Grey Matter
32	urine	3	Blood	113	cerebral falx	14	Dura
33	feces	18	Fat	114	temporal lobes	8	Brain Grey Matter
34	testes	40	Testis	115	fourth ventricle	12	Cerebrospinal Fluid
35	prostate	33	Prostate	116	frontal portion eye	17	Eye Vitrous Humor
37	rectum	23	Large Intestine	117	parietal lobes	8	Brain Grey Matter
39	diaphragm	13	Diaphragm	118	amygdala	9	Brain White Matter
40	bladder	46	Urinary Bladder	119	eye	17	Eye Vitrous Humor
63	lesion	3	Blood	120	globus pallidus	9	Brain White Matter
70	dense of axis	3	Blood	121	lens	16	Eye Lens
71	jaw bone	4	Bone	122	cerbral aqueduct	12	Cerebrospinal Fluid
72	parotid gland	42	Thyroid Gland	123	lateral ventricles	12	Cerebrospinal Fluid
74	lacrimal gland	42	Thyroid Gland	124	prefrontal cortex	8	Brain Grey Matter
75	spinal canal	37	Spinal Cord	125	teeth	44	Tooth

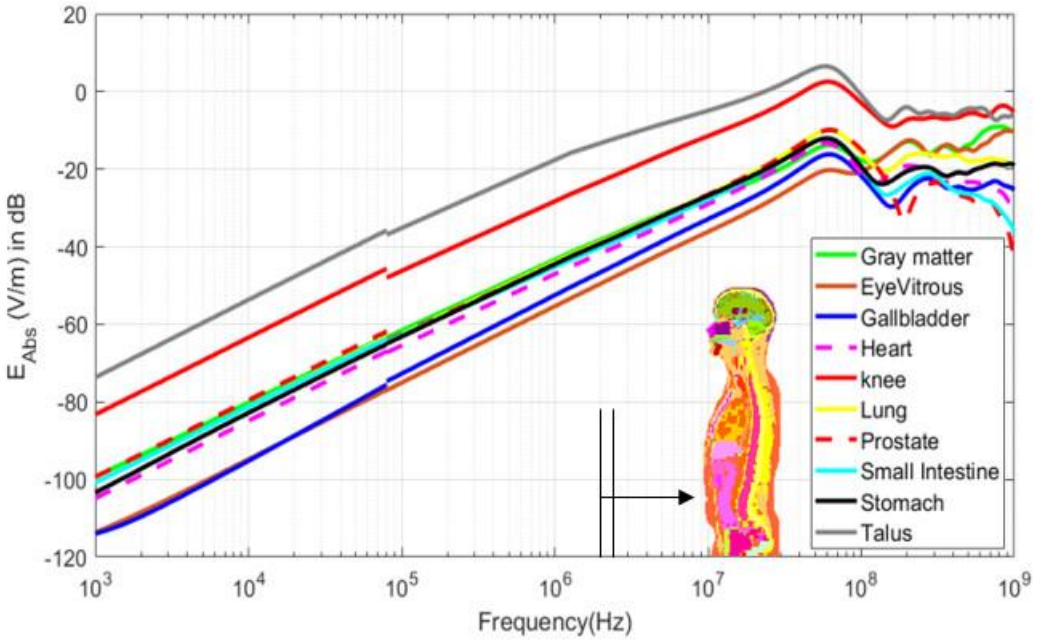

Fig. 3. Results of induced electric fields in several specific tissues in *two* simulation intervals

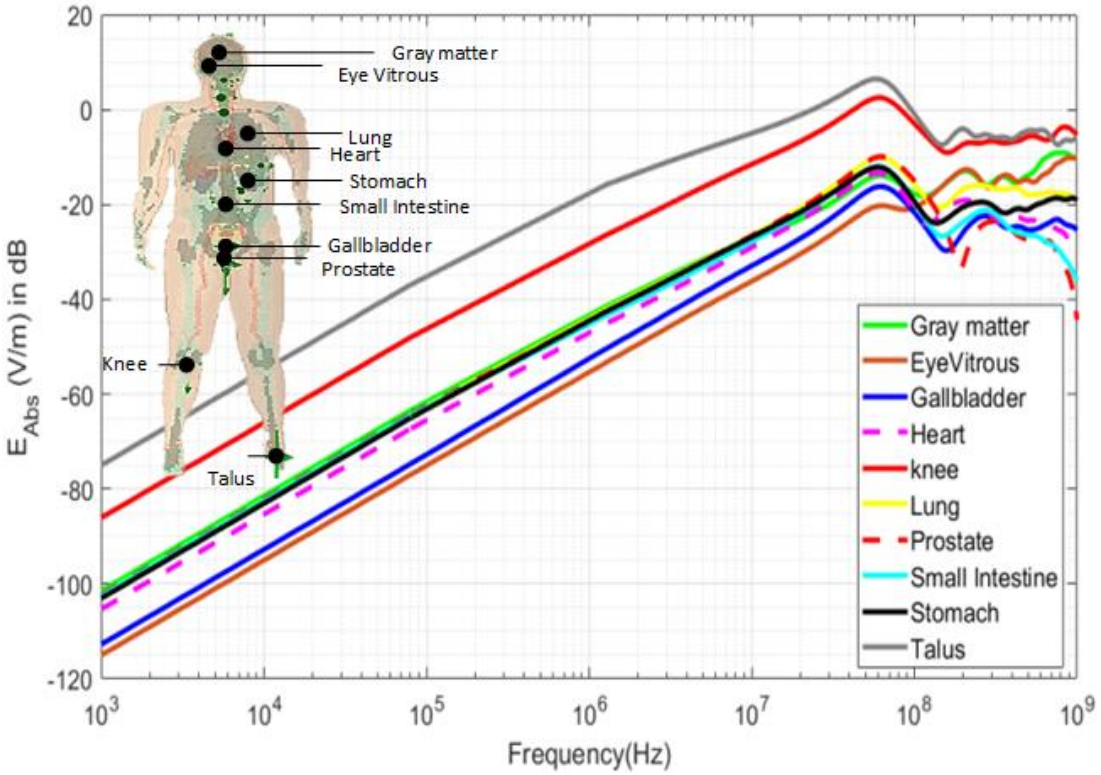

Fig. 4. Final results of induced electric fields in selected tissues.

This can also be analytically deduced from the solution of the Laplace's equation for electric field inside a conducting sphere when placed inside a uniform electric field as shown in the appendix. Consequently, the electric field below 100 kHz is obtained by extending the fields just above 100 kHz down with a slope of 20dB/dec. The final result is given in Fig.4.

The results of the electric field generated by the body scale analysis in Fig. 4 indicate that the peak of electric field penetration in the body occurs at around 70 MHz (65 MHz), which is the same as the well-known resonant frequency of the body. At lower frequencies, the displacement of free charges in response to the initial induced electric field and the creation

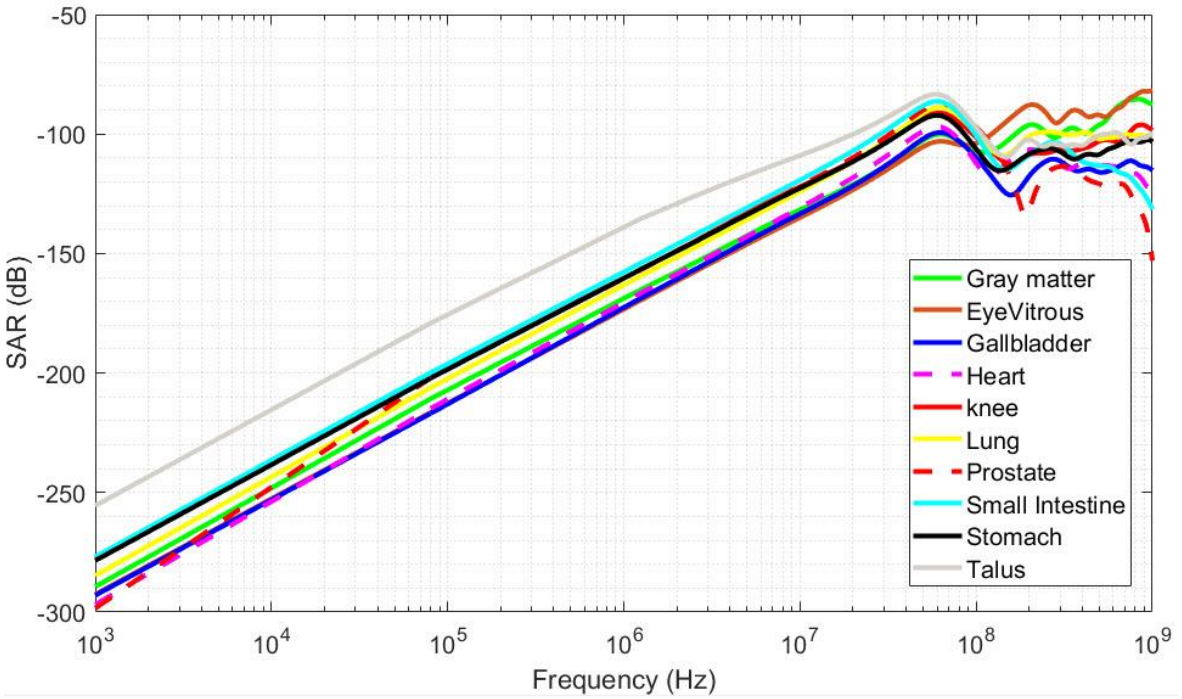

Fig. 5. Final results of specific absorption rate (SAR) in selected tissues. Please note the dB scale, which is 10log10(SAR(W/Kg)) shown on the vertical scale for the corresponding Electric field intensities in figure 4.

of a secondary field opposite to the radiation field reduces the induced field within the body. At frequencies higher than the resonance frequency, with increasing tissue loss, the energy of the radiation field is absorbed at the body surface, thereby reducing the electric field strength at deeper points within the body. It can be seen that the difference between tissues can be as high as 30 dB, and that tissues with lower water content (e.g. bones, knee) can generally have higher induced electric fields. High water content tissues such as the eye vitreous humor have generally lower induced electric fields.

The specific rate of absorption (SAR) has been estimated for these tissues in Fig.5. Computation of SAR has been done based on (2);

$$SAR = \frac{\sigma E^2}{2\rho} \tag{2}$$

where the conductivity is a frequency dependent parameter dependent on tissue type, and mass density has been assumed an average constant for all tissues. It is observedin Fig.5 that power dissipation tends to be higher for low-water-content tissues where the electric field has been higher.

As a final note, human body models can be of use esp. for high frequency applications. However, care must be practiced when applying such models for low frequency applications. The reason is two-fold: first, the low frequency electrical properties of tissues are generally harder to evaluate experimentally mostly due to electrode polarization error [11-12]. Second, the voxel models often neglect extremely thin basal membranes or epithelial layers that might act as barrier to ionic currents at lower frequencies. At higher frequencies, the capacitive effects of these layers might be considered as shorted out, and contribute little to the electric field results.

4. Conclusion

In this paper we presented a voxel model of the human body with voxel size of 3.6 mm and 46 types of tissue properties. All electrical properties of tissues are calculated and prepared in a proper format for simulation in CST software. Evaluation of frequency response for the induced electric fields in some organs and tissues has been demonstrated as an example of the application of this model. It has been seen that the electric field intensity in different tissues can have differences up to about 30 dBs, with low-water-content tissues showing stronger internal electric fields. The model is freely available at www.bioelectromag.ir.

Appendix

The field inside a sphere within a medium can be represented as:

$$\frac{E_{body}}{E_{inc}} = \frac{3\varepsilon_{ra}}{2\varepsilon_{ra}+\varepsilon_{rb}} \tag{A.1}$$

where the ambient environment around the body is denoted by *a* and the sphere denoted by *b*, and ε_r denotes relative complex permittivity. At lower frequencies the conductivity is dominant over dielectric permittivity and the complex permittivity $\boldsymbol{\varepsilon}_{rb} = \boldsymbol{\varepsilon}_r' - j(\boldsymbol{\varepsilon}_r'' + \boldsymbol{\sigma}_i/\boldsymbol{\omega}\boldsymbol{\varepsilon}_0)$ can be approximated by the term corresponding to conductivity

alone, thus arriving at (2).

$$\frac{E_{body}}{E_{inc}} = \frac{3}{2 + \frac{\sigma_i}{\omega\varepsilon_0}} \cong \frac{3\omega\varepsilon_0}{\sigma_i} \propto f \qquad (A.2)$$

5. References:

[1] C.M. Furse, Bioelectromagnetic Dosimetry: Simulating Electromagnetic Fields in the Human Body, in: The World of Applied Electromagnetics, Springer, 2018, pp. 351-368.

[2] M.-C. Gosselin, E. Neufeld, H. Moser, E. Huber, S. Farcito, L. Gerber, M. Jedensjö, I. Hilber, F. Di Gennaro, B. Lloyd, Development of a new generation of high-resolution anatomical models for medical device evaluation: the Virtual Population 3.0, Physics in Medicine & Biology, 59(18) (2014) 5287.

[3] D. Jones, A realistic anthropomorphic phantom for calculating organ doses arising from external photon irradiation, Radiation Protection Dosimetry, 72(1) (1997) 21-29.

[4] J.W. Massey, A.E. Yilmaz, AustinMan and AustinWoman: High-fidelity, anatomical voxel models developed from the VHP color images, in: 2016 38th Annual International Conference of the IEEE Engineering in Medicine and Biology Society (EMBC), IEEE, 2016, pp. 3346-3349.

[5] P. Dimbylow, Development of the female voxel phantom, NAOMI, and its application to calculations of induced current densities and electric fields from applied low frequency magnetic and electric fields, Physics in Medicine & Biology, 50(6) (2005) 1047.

[6] P. Dimbylow, W. Bolch, Whole-body-averaged SAR from 50 MHz to 4 GHz in the University of Florida child voxel phantoms, Physics in Medicine & Biology, 52(22) (2007) 6639.

[7] T. Nagaoka, S. Watanabe, K. Sakurai, E. Kunieda, S. Watanabe, M. Taki, Y. Yamanaka, Development of realistic high-resolution whole-body voxel models of Japanese adult males and females of average height and weight, and application of models to radio-frequency electromagnetic-field dosimetry, Physics in Medicine & Biology, 49(1) (2003) 1.

[8] Y.H. Na, B. Zhang, J. Zhang, P.F. Caracappa, X.G. Xu, Deformable adult human phantoms for radiation protection dosimetry: anthropometric data representing size distributions of adult worker populations and software algorithms, Physics in Medicine & Biology, 55(13) (2010) 3789.

[9] T. Nagaoka, S. Watanabe, Postured voxel-based human models for electromagnetic dosimetry, Physics in Medicine & Biology, 53(24) (2008) 7047

[10] I.G. Zubal, C.R. Harrell, E.O. Smith, Z. Rattner, G. Gindi, P.B. Hoffer, Computerized three-dimensional segmented human anatomy, Medical physics, 21(2) (1994) 299-302.

[11] C. Gabriel, S. Gabriel, y.E. Corthout, The dielectric properties of biological tissues: I. Literature survey, Physics in medicine & biology, 41(11) (1996) 2231

[12] S. Gabriel, R.W. Lau and C. Gabriel, The dielectric properties of biological tissues: II. Measurements in the frequency range 10 Hz to 20 GHz, Phys. Med. Biol. 41 (1996), 2251-2269..

[13] S. Gabriel, R. Lau, C. Gabriel, The dielectric properties of biological tissues: III. Parametric models for the dielectric spectrum of tissues, Physics in medicine & biology, 41(11) (1996) 2271.

HOW TO CITE THIS ARTICLE

M. Rajaei Golsefidi, Z. Hajizadeh Bakhtiary, E. Sharifi, M. Saviz, R. Faraji-Dana, Development of a free anthropomorphic voxel model of human body for wide-band computational electromagnetics dosimetry, AUT J. Elec. Eng., 52(2) (2020) 187-192.

DOI: 10.22060/eej.2020.18179.5346